Available online at www.sciencedirect.com
SCIENCE DIRECT®
PERGAMON
International Journal of Multiphase Flow 29 (2003) 411–434
International Journal of Multiphase Flow
www.elsevier.com/locate/ijmulflow

Modeling of Taylor bubble rising in a vertical mini noncircular channel filled with a stagnant liquid

Q. Liao [a,b], T.S. Zhao [a,*]

[a] *Department of Mechanical Engineering, The Hong Kong University of Science and Technology, Clear Water Bay, Kowloon, Hong Kong, China*
[b] *Institute of Engineering Thermophysics, Chongqing University, Chongqing, 400044 China*

Received 15 May 2002; received in revised form 12 November 2002

Abstract

This paper presents a theoretical model that predicts the drift velocity of an elongated bubble (a Taylor bubble) in vertical mini triangular and square channels closed at the bottom and filled with a stagnant liquid. To facilitate the analysis, the bubble profile is divided into three zones along bubble length: the front meniscus zone, the uniform film zone in the middle of the bubble, and the rear meniscus zone. The model takes into account the effects of capillary pressure, induced by the interfacial curvature variations along bubble length, gravity, and viscous force. The interfacial profiles and the bubble drift velocities are determined by solving the conservation equations of the momentum of the liquid phase coupled with the equations of the force balance at the bubble interface. The predicted drift velocities of the bubble in both mini triangular and square channels are found to be favorably in an agreement with the experimental data in the literature. It has been revealed that the drift velocities in the triangular channel are substantially higher than those in the square channel having the same hydraulic diameter. The influences of channel size and the physical properties of the fluid on the bubble drift velocities are also examined. Finally, respective correlations for predicting the bubble drift velocities in both mini triangular and square channels are developed in terms of appropriate dimensionless parameters.

Keywords: Taylor bubbles; Two-phase flow; Drift velocity; Microchannels

* Corresponding author. Tel.: +852-2358-8647; fax: +852-2358-1543.
E-mail address: metzhao@ust.hk (T.S. Zhao).

0301-9322/03/$ - see front matter
doi:10.1016/S0301-9322(03)00004-1

1. Introduction

Gas slug or Taylor bubble flow is a type of gas–liquid channel flow characterized by the existence of large asymmetric bullet-shaped bubbles, which occupy almost the entire cross-section of the channel with a rounded leading edge and has a length of several times the channel hydraulic diameter. The study of the behavior of Taylor bubbles is of fundamental importance in gas–liquid two-phase flows in channels and is particularly relevant to the slug flow regime that occurs at intermediate void fractions with relatively low liquid flow rates. Slug flow is frequently encountered during the immiscible displacement of viscous oil in the porous rock of an oil-wet reservoir, during the displacement of water from a natural gas reservoir during gas production, in chemical and nuclear reactors, and numerous heat transport systems in which a phase change takes place. In this work, we are concerned with the study of the motion of an isolated elongated bubble formed in miniature channels with stagnant liquids, with a special focus on the prediction of the drift velocity of the bubble.

A number of experimental investigations of the rising behavior of Taylor bubbles in circular tubes have been reported. Zukoski (1966) conducted an experimental investigation of the motion of long bubbles in a closed tube and clarified the influence of viscosity and surface tension on the bubble velocity. Collins (1967) performed experiments to study the effect of a cylindrical boundary on the velocity of rising large gas bubbles. To describe the rising of large inviscid bubbles in tubes, White and Beardmore (1962) expressed the terminal velocity of gas slugs in terms of a dimensionless parameter, the Froude number, $Fr = V_b[\rho_l/(\Delta\rho g d)]^{1/2}$, which depended on the Eötvös number, $E\ddot{o} = \Delta\rho g d^2/\sigma$, and the Morton number, $Mo = g\mu_l^4\Delta\rho/\rho_l^2\sigma^3$, where V_b is the terminal velocity of the bubble, $\Delta\rho$ the two-phase density difference, σ the surface tension, μ the dynamic viscosity, d the inside diameter of tube, and the subscript "l" represents the liquid phase. For low viscosity and high surface tension systems such as the air–water two-phase flow in a sufficiently large-diameter tube, the Morton number is rather small (on the order of 10^{-10}) compared with Eötvös number ($E\ddot{o} = 100$), and the terminal velocity of the gas slugs thus depends on the Eötvös number, $E\ddot{o}$, only, i.e.,

$$V_b = 0.35[\Delta\rho g d/\rho_L]^{1/2} \tag{1}$$

which indicates that the rising velocity of the bubble in a vertical tube with a large-diameter is proportional to $(gd)^{1/2}$. Similar conclusions were also drawn by Zukoski (1966), Tung and Parlange (1976), and Kataoka et al. (1987). For a moderate size tube, Tung and Parlange (1976) proposed that the rising velocity of the bubble could be determined by

$$V_b^2/gd = 0.272 - 0.472\sigma/\rho g d^2. \tag{2}$$

The last term on the right-hand side of Eq. (2) indicates that surface tension becomes significant in small tubes. For a sufficiently small-diameter tube, $E\ddot{o} \leqslant 3.37$, the gas slug velocity becomes zero. Recently, Polonsky et al. (1999) experimentally studied the motion of a single Taylor bubble propagating in a vertical pipe in a stagnant liquid and discussed the relation between the motion of a Taylor bubble and the velocity field in front of the bubble. Tudose and Kawaji (1999) used a solid model of a Taylor bubble placed in a vertical tube to experimentally investigate the acceleration mechanism of a Taylor bubble. They found the Taylor bubble acceleration in slug flow

comes from the reduction in drag force changes in the nose shape and in the lateral displacement of the bubble from the vertical pipe axis.

Some experimental investigations on Taylor bubbles in mini noncircular channels have been reported. Monde (1990) measured the liquid film thickness between the bubble and the solid wall as the bubble rose in a vertical rectangular channel with a narrow space of 2.0 mm. Caetano et al. (1992) studied the rising velocities of Taylor bubbles in a vertical concentric and fully eccentric annuli filled with stagnant liquids. Kolb and Cerro (1991) conducted a visual study of a long bubble moving in mini square channels under the combination effects of gravity and/or air pressure. Their results showed that with the increase of the Ca number, $Ca = (\mu V_b)/\sigma$, an axisymmetric bubble and a nonaxisymmetric bubble occurred subsequently in mini square channels. The transition from a nonaxisymmetrical bubble to axisymmetrical bubble was found to occur at $Ca \approx 0.1$. The bubble interface in the axial plane was found to consist of three regions: a cap region, a transition region, and a uniform region. The effect of the channel shape became more pronounced for small Ca numbers. More recently, Bi and Zhao (2001) investigated elongated bubble behavior in miniature noncircular channels including triangular, square, and rectangular channels filled with a stagnant liquid. They found that in the triangular and rectangular channels, elongated bubbles always rose upward even though the hydraulic diameter of the tube was as small as 0.866 mm. This peculiar behavior was attributed to the fact that the corners of the noncircular channels were always in the liquid phase owing to the capillary force. As such, a continuous liquid phase could be maintained and thus, the buoyancy force existed all the time to drive the bubble moving upwards. They measured the drift velocity of long bubbles in vertical noncircular channels and found that Eq. (2) proposed by Tung and Parlange (1976) for small round tubes was not applicable in predicting the drift velocity in miniature noncircular channels.

Bretherton (1961) was perhaps among the first to perform a theoretical analysis of a long bubble moving steadily in both horizontal and vertical circular tubes. For low capillary numbers, $Ca = (\mu V_b)/\sigma$, he obtained an approximate solution by the matched asymptotic expansion method. In the asymptotic analysis of a long bubble flowing in horizontal tubes, he assumed that the bubble profile consisted of four zones: the front and rear meniscus zones with constant curvature; the uniform film zone, where the free surface is impacted by uniform pressure with no tangential stress, between the front and rear meniscus zones; the transition zones between the uniform film zone and the front and rear meniscus zones, in which both the viscous force and the surface tension dominate the liquid-phase flow and the 'lubrication approximation' was used to describe the flow of a sufficiently small capillary number. Bretherton also performed experiments to validate his asymptotic results and found reasonable agreement for $Ca < 10^{-4}$ but the measured value of the effective film thickness greatly exceeded the theoretical results for smaller capillary numbers. Bendiksen (1985) and Nickens and Yannitell (1987) used potential flow theory to study the shape and the rising velocity, respectively, of larger bubbles in vertical tubes with a stagnant liquid. Reinelt (1987) determined numerically the shape and the rising velocity of a long bubble in a vertical tube and extended the relationship between the Bond number and the capillary number to a region where the perturbation expansion is no longer valid. Martinez and Udell (1989) conducted a boundary integral analysis of the creeping motion of a long inviscid bubble in a horizontal liquid filled tube. Employing the volume of fluid method, Tomiyama et al. (1996) numerically investigated a Taylor bubble moving a vertical pipe filled with a stagnant liquid. Their

numerical results on the terminal rising velocities and the bubble shapes were in good agreement with the experimental data.

Relatively few theoretical and numerical investigations have been conducted on the motion of long bubbles in mini noncircular channels. Legait (1983) performed a static hydraulic analysis in order to estimate the pressure drop that drives a bubble through a square capillary. Ransohoff and Radke (1988) numerically studied the problem of wetting liquid flow with low Reynolds numbers in a noncircular capillary occupied predominantly by a nonwetting gas phase. Ratulowski and Chang (1989) established an arc-length-angle formulation of a composite lubrication equation to compute the pressure drop and the wetting film thickness of isolated bubbles and bubble trains moving in horizontal circular and square capillaries. Focusing on the coating inside capillaries with square cross-sections, Kolb and Cerro (1993a) obtained the solution, developed as an infinite series of harmonic polynomials, for film flow in the space between a circular bubble and a square tube. Furthermore, Kolb and Cerro (1993b) theoretically analyzed the Taylor–Bretheron problem for a long bubble displacing a viscous fluid in tubes with square cross-sections. The analysis considered the effects of viscous, capillary, and gravity forces. Wong et al. (1995a,b) theoretically studied the pressure-driven motion of long bubbles in horizontal polygonal capillaries. Furthermore, Thulasidas et al. (1995) developed a theoretical method to predict the bubble size and shape, the bubble velocity, and the volume fraction of the gas for bubble-train flow in capillaries with square cross-sections.

Theoretical investigations of rising Taylor bubbles in mini noncircular channels filled with a stagnant liquid are rather scarce. Caetano et al. (1992) and Das et al. (1998) modeled the rising behavior of Taylor bubbles in vertical concentric and fully eccentric annuli, respectively. More recently, Yang et al. (2001) employed the lattice-Boltzmann method to simulate the rising velocities of Taylor bubbles in narrow channels.

In the present paper, we report on a theoretical investigation of the drift velocity of an elongated bubble moving upwards in vertical mini equilateral triangular channels and square channels under the effect of buoyancy. The bubble interface profile along its length is divided into three zones along bubble length: the front meniscus zone, the rear meniscus zone, and the uniform film zone. The effects of the liquid viscous flow, the surface tension, and buoyancy are taken into account in the model. It is found that the bubble drift velocity is substantially higher in equilateral triangular channels than in square channels having the same hydraulic diameters. The influences of channel size and the physical properties of the fluid on the drift velocity are also examined. Based on our numerical solutions, two simple correlations are proposed to predict bubble drift velocities in equilateral triangular channels and square channels.

2. Mathematical formulation

Consider an isolated, elongated gas bubble (a Taylor bubble) surrounded by a liquid in a vertical mini channel with an equilateral triangular cross-section (see Fig. 1) or a square cross-section (see Fig. 2) with a sidewall length b. Under the condition in which the bottom end of the channel is sealed, the Taylor bubble drifts upward in the channel owing to the effect of buoyancy, while the surrounding liquid moves downward to replenish the space vacated by the bubble in the rear region of the bubble. The bubble interface profile and the drift velocity are in general

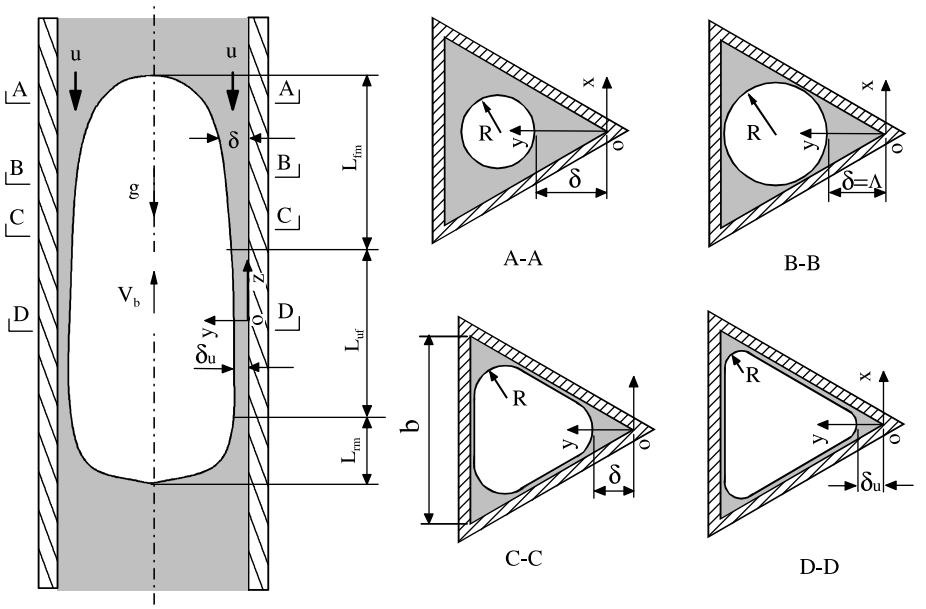

L_{fm}: Front meniscus zone
L_{uf}: Uniform film zone
L_{rm}: Rear meniscus zone

Fig. 1. Schematic of the physical problem in triangular channels.

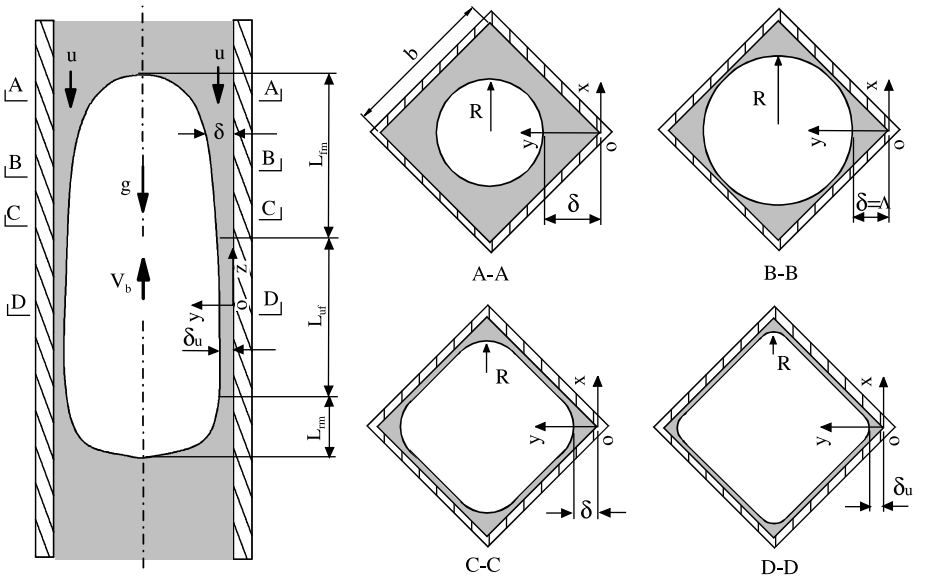

L_{fm}: Front meniscus zone
L_{uf}: Uniform film zone
L_{rm}: Rear meniscus zone

Fig. 2. Schematic of the physical problem in square channels.

dependent on the hydrodynamic interaction between the bubble and its surrounding liquid flow. In this work, we consider only bubbles moving at a constant speed, V_b characterized by the capillary number, $Ca = (\mu V_b)/\sigma$. In the previous studies on Taylor bubbles in circular tubes (e.g., Bretherton, 1961; Martinez and Udell, 1989; Ratulowski and Chang, 1989) with small $Ca = (\mu V_b)/\sigma$, it was usually assumed that the typical profile of the Taylor bubble might be divided into five zones along bubble length: the front meniscus zone at the top, the rear meniscus zone at the bottom, the uniform film zone in the middle of the bubble, as well as the two transition zones (one from the uniform film zone to the front meniscus zone, and the other from the uniform film zone to the rear meniscus zone). Such zone divisions of the bubble profiles in circular tubes were verified experimentally by Goldsmith and Mason (1963). For very long bubbles, the effect of the two transition zones becomes less important and can be subsumed by the uniform film zone. It was found by Bi and Zhao (2001) that Taylor bubbles in mini channels with sharp corners were substantially elongated as compared with those in large circular tubes. Thus, for the mini noncircular channels considered in this work, it seems reasonable to ignore the transition zones and divide the Taylor bubble into three zones: the front meniscus zone at the top, the rear meniscus zone at the bottom, and the uniform film zone in the middle, as shown in Figs. 1 and 2. Several typical liquid/gas interfacial profiles at selected cross-sections are illustrated on the right side of Fig. 1 or Fig. 2. Near the bubble cap, the gas phase occupies the channel core, represented by a circle with radius R, while the remaining area of the cross-section is filled with the liquid (see cross-section A–A), where δ represents the distance from the channel corner tip to the gas–liquid interface. This is refereed to as the gas/liquid interface location in this work. Moving downward along the bubble, the area of the gas phase becomes progressively larger (R increases) and the corresponding liquid area becomes smaller (δ decreases). At the cross-section B–B, the gas core just takes the shape of an inner tangential circle of the triangle. Further downward to the cross-section C–C, the gas circle is deformed as the liquid film forms along the sidewall. Owing to the meniscus effect induced by the sharp corners of the channel, the liquid film becomes progressively thinner in the uniform film zone. For convenience, we refer to the gas core flow at the cross-sections A–A and B–B as the circular gas flow, whereas the gas core flow at the cross-sections C–C and D–D is referred to as the deformed gas flow. The bubble profiles over the above selected cross-sections were verified by the flow visualization by Kolb and Cerro (1991). Similar descriptions on the bubble profile were also made by Ratulowski and Chang (1989), Kolb and Cerro (1993b), and Wong et al. (1995a,b) for studying long bubbles moving in square channels.

2.1. Geometric parameters

Before analyzing the hydrodynamic transport in the aforementioned three distinctive zones, we first obtain some key geometric relationships by referring to Figs. 1–3 for both the triangular and the square channels. It is assumed that the contact angle of the liquid at the channel wall is zero, which means that the arc-shaped liquid–gas interface is tangential to the channel sidewall. At the cross-section B–B (see Fig. 1 for the triangular channel and Fig. 2 for the square channel), where the gas core takes the shape of an inner tangential circle of the channel, the distance from the channel corner tip to the gas–liquid interface, δ, is related to the sidewall length, b, and the channel corner angle, α, ($\alpha = \pi/3$ for the equilateral triangular channel and $\alpha = \pi/2$ for the square channel) as follows:

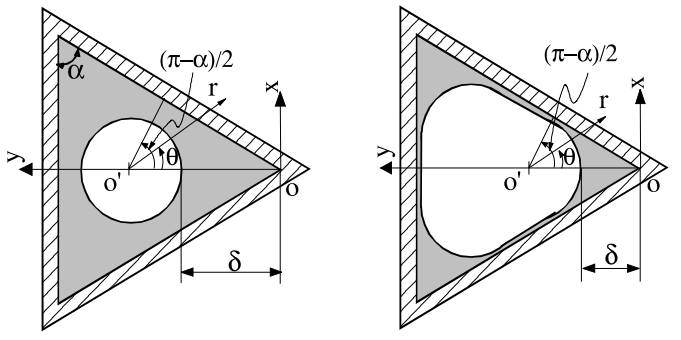

(a) Triangular channel

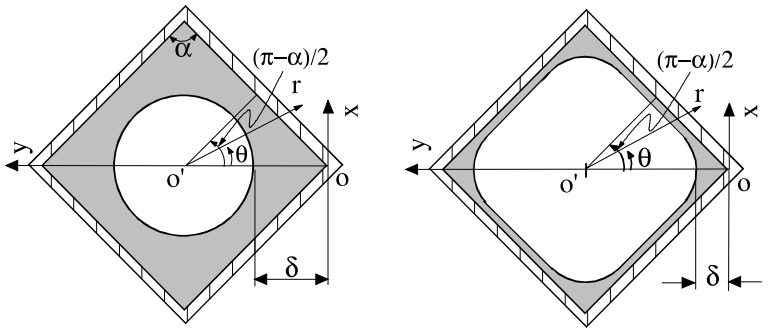

(b) Square channel

Fig. 3. Coordinates for computing the liquid flow field.

$$\delta = \Lambda = \frac{b}{2}\left[\frac{1}{\cos(\alpha/2)} - \tan(\alpha/2)\right]. \tag{3}$$

Thus, for the case of the deformed gas flow ($\delta \leqslant \Lambda$) (see Fig. 3a for the triangular channel and Fig. 3b for the square channel), the meniscus radius, R, is related to the distance from the corner tip to the liquid/gas interface, δ, by

$$R = \delta \sin(\alpha/2)/[1 - \sin(\alpha/2)], \tag{4}$$

while, for the case of the circular gas flow $\delta > \Lambda$,

$$R = \frac{b}{2\cos(\alpha/2)} - \delta. \tag{5}$$

The area occupied by the liquid, A_1 in the one-sixth portion of the cross-sectional area of the triangular channel or the one-eighth portion of the cross-sectional area of the square channel is given by

$$A_l = \frac{R^2\left[2\cot\left(\frac{\alpha}{2}\right) - (\pi - \alpha)\right]}{4} \tag{6}$$

for $\delta \geqslant \Lambda$

$$\text{and} \quad A_l = \frac{b^2 \tan\left(\frac{\alpha}{2}\right) - 2(\pi - \alpha)R^2}{8} \tag{7}$$

for $\delta < \Lambda$. The hydraulic diameter, D_h of the entire channel is defined as

$$D_h = \tfrac{2}{3} b \sin\alpha \tag{8}$$

for the equilateral triangular channel, and

$$D_h = b \tag{9}$$

for the square channel.

2.2. The force balance at the bubble interface

For the steadily creeping motion of a long inviscid bubble in the channel filled with an incompressible liquid, we assume that the gas viscosity is negligible and the interfacial tension, σ, is constant. As a result, the viscous stress tangential to the bubble interface vanishes and the bubble profile is determined by the Young–Laplace equation:

$$p_g - p_l = p_c, \tag{10}$$

where p_c is the capillary pressure, p_g and p_l represent the gas and the liquid pressure, respectively. The capillary pressure, p_c, is related to the two principal radii of the interfacial curvature, r_1 and r_2 by

$$p_c = p_g - p_l = \sigma\left(\frac{1}{r_1} + \frac{1}{r_2}\right) = \sigma\left\{\frac{\mathrm{d}^2\delta}{\mathrm{d}z^2}\Big/\left[1 + \left(\frac{\mathrm{d}\delta}{\mathrm{d}z}\right)^2\right]^{3/2} + 1\Big/R\left[1 + \left(\frac{\mathrm{d}\delta}{\mathrm{d}z}\right)^2\right]\right\}. \tag{11}$$

Differentiating Eq. (11) with respect to z, and assuming that the pressure within the bubble is uniform, $\mathrm{d}p_g/\mathrm{d}z = 0$, we obtain

$$\frac{\mathrm{d}p_l}{\mathrm{d}z} = -\frac{\mathrm{d}p_c}{\mathrm{d}z} = -\sigma\frac{\mathrm{d}}{\mathrm{d}z}\left\{\frac{\mathrm{d}^2\delta}{\mathrm{d}z^2}\Big/\left[1 + \left(\frac{\mathrm{d}\delta}{\mathrm{d}z}\right)^2\right]^{3/2} + 1\Big/R\left[1 + \left(\frac{\mathrm{d}\delta}{\mathrm{d}z}\right)^2\right]^{1/2}\right\}. \tag{12}$$

Eq. (12) is applicable in the entire bubble, i.e., the front meniscus, the rear meniscus, and the uniform film zone. It is clear from Eq. (12) that once the local liquid pressure gradient is obtained, the bubble profile can be determined by solving Eq. (12) subject to the following boundary conditions:

$$\delta = \delta_u: \quad \frac{\mathrm{d}\delta}{\mathrm{d}z} = 0, \ \frac{\mathrm{d}^2\delta}{\mathrm{d}z^2} = 0, \ \frac{\mathrm{d}^3\delta}{\mathrm{d}z^3} = 0 \tag{13}$$

where δ_u represents the location of the bubble interface in the channel corner in the uniform film zone (see Fig. 1). The local liquid pressure gradient around the bubble is obtained based on the procedures described next.

2.3. The liquid viscous flow around the bubble

In dealing with the liquid flow around the bubble, as in the previous studies (Bretherton, 1961; Martinez and Udell, 1989; Schwartz et al., 1986; Stebe and Barthes-Biesel, 1995), we make the following assumptions: (1) the liquid motion in the liquid-phase zone around the bubble is assumed to be an incompressible, fully developed laminar flow with constant fluid properties; (2) the inertial force due to the motion of the liquid at small Reynolds numbers is neglected; (3) the viscous shear stress at the interface is assumed to be zero; and (4) the liquid flow is assumed to be one-dimensional in the channel axial direction. Considering the fact that for the case of the deformed gas flow (see Fig. 3) the liquid film along the sidewall is extremely thin as compared with the corner regions, we further assume that the flow of the flat liquid film along the sidewall is negligibly small. Kolb and Cerro (1993a) theoretically analyzed the motion of air bubbles in a square channel filled with a stagnant liquid and found that the liquid flow over the four corner regions exceeds 95% of the total flow rates across the cross-section of the channel.

Due to the fact that the liquid flow across the cross-section is symmetric with respect to the channel centerline, we consider one-sixth portion of the cross-section of the channel only. Referring to the polar coordinate shown in Fig. 3, the axial equation of the momentum conservation for the liquid flow is given by

$$\frac{\partial^2 u}{\partial r^2}+\frac{1}{r}\frac{\partial u}{\partial r}+\frac{1}{r^2}\frac{\partial^2 u}{\partial \theta^2}-\frac{1}{\mu}\left[\frac{\mathrm{d}p_\mathrm{l}}{\mathrm{d}z}-(\rho_\mathrm{l}-\rho_\mathrm{g})g\right]=0, \tag{14}$$

where the subscripts "l" and "g" represent the liquid phase and gas phase, respectively. The corresponding boundary conditions are

$$\theta=0,\quad \frac{\partial u}{\partial \theta}=0;\qquad \theta=\frac{\pi-\alpha}{2},\quad \frac{\partial u}{\partial \theta}=0, \tag{15}$$

$$r=R,\quad \frac{\partial u}{\partial r}=0;\qquad r=\frac{b\tan\left(\frac{\alpha}{2}\right)}{2\sin\left(\frac{\alpha}{2}+\theta\right)},\quad u=0. \tag{16}$$

Eq. (14) is a second-order linear and inhomogeneous partial differential equation and can be solved based on the procedures described in the subsequent paragraphs.

Introducing the following intermediate variables:

$$G=\frac{1}{\mu}\left[\frac{\mathrm{d}p_\mathrm{l}}{\mathrm{d}z}-(\rho_\mathrm{l}-\rho_\mathrm{g})g\right], \tag{17}$$

$$u(r,\theta)=\frac{Gr^2}{4}+\tilde{u}(r,\theta) \tag{18}$$

$$\text{and}\quad J(\theta)=\frac{b\tan\left(\frac{\alpha}{2}\right)}{2\sin\left(\frac{\alpha}{2}+\theta\right)}, \tag{19}$$

we can transform Eq. (14) and the boundary conditions given by Eqs. (15) and (16) into

$$\frac{\partial^2 \tilde{u}}{\partial r^2}+\frac{1}{r}\frac{\partial \tilde{u}}{\partial r}+\frac{1}{r^2}\frac{\partial^2 \tilde{u}}{\partial \theta^2}=0, \tag{20}$$

$$\theta = 0, \quad \frac{\partial \tilde{u}}{\partial \theta} = 0; \qquad \theta = \frac{\pi - \alpha}{2}, \quad \frac{\partial \tilde{u}}{\partial \theta} = 0, \tag{21}$$

$$r = R, \quad \frac{\partial \tilde{u}}{\partial r} = -\frac{GR}{2}, \tag{22}$$

$$r = J(\theta), \tilde{u} = -\frac{GJ^2(\theta)}{4}. \tag{23}$$

To solve Laplace's equation (20), we assume

$$\tilde{u}(r, \theta) = \Phi(r) \cdot \Theta(\theta). \tag{24}$$

Substituting Eq. (24) into Eq. (20) subject to the boundary conditions given by Eq. (21), we obtain the eigenvalue function as

$$\Theta_i(\theta) = \cos(\beta_i \theta), \tag{25}$$

where β_i is the eigenvalue, $\beta_i = 3i$, $i = 0, 1, 2, \ldots, n$.

Similarly, the solutions in the r direction are obtained as follows,

$$\Phi_i(r) = A + B \ln r, \quad i = 0 \tag{26}$$

and

$$\Phi_i(r) = C_i r^{\beta_i} + D_i r^{-\beta_i}, \quad i = 1, 2, \ldots, n. \tag{27}$$

Since the Laplace's equation is linear and homogenous, the general solution can be expressed by

$$\tilde{u}(r, \theta) = \sum_{i=0}^{N} \Phi_i(r) \cdot \Theta_i(\theta) = A + B \ln r + \sum_{i=1}^{N} (C_i r^{\beta_i} + D_i r^{-\beta_i}) \cos(\beta_i \theta), \tag{28}$$

where A, B, C_i, D_i are constants to be determined as discussed below.

Substituting the boundary condition given by Eq. (22) into Eq. (28), we have

$$B = -\frac{GR^2}{2} \tag{29}$$

and

$$D_i = C_i R^{2\beta_i}. \tag{30}$$

Then, Eq. (28) can be rewritten as

$$\tilde{u}(r, \theta) = A - \frac{GR^2}{2} \ln r + \sum_{i=1}^{N} C_i (r^{\beta_i} + R^{2\beta_i} r^{-\beta_i}) \cos(\beta_i \theta), \tag{31}$$

where the constants A and C_i are determined from the boundary condition given by Eq. (23). The boundary condition, Eq. (23), can also be expressed as

$$r = r_j = J(\theta_j), \qquad \tilde{u} = -\frac{GJ^2(\theta_j)}{4}. \tag{32}$$

Here the suffix j denotes the value of a point on the channel boundary. To apply this boundary condition to the general solution, Eq. (31), we have

$$\widetilde{A} + \sum_{i=1}^{N} \widetilde{C}_i [J^{\beta_i}(\theta_j) + R^{2\beta_i} J^{-\beta_i}(\theta_j)] \cos(\beta_i \theta) = \frac{2R^2 \ln J(\theta_j) - J(\theta_j)}{4}, \tag{33}$$

where $\widetilde{A} = A/G$ and $\widetilde{C}_i = C_i/G$. Eq. (33) represents $\widetilde{A}$ and $\widetilde{C}_i$, a total of $n = N + 1$ unknown coefficients. The values of $J(\theta_j)$ and θ_j are provided for m points at the channel boundary so that m equations are available for n unknowns. The problem essentially reduces to that of solving the following equation with proper elements of the matrix $\boldsymbol{F}$ and the vector $\boldsymbol{Y}$ from Eq. (33), i.e.,

$$\boldsymbol{F}\boldsymbol{X} = \boldsymbol{Y}\ , \tag{34}$$

where $\boldsymbol{X} = (X_1, \ldots, X_i, \ldots, X_n)^{\mathrm{T}}$ is a vector whose elements are to be determined and X_i correspond to the unknown series coefficients $\widetilde{A}$ and $\widetilde{C}_i$ in Eq. (33). The vector $\boldsymbol{Y} = (Y_1, \ldots, Y_j, \ldots, Y_m)^{\mathrm{T}}$ is known for the m specified boundary points on the channel periphery, i.e.,

$$Y_j = \frac{2R^2 \ln J(\theta_j) - J(\theta_j)}{4}. \tag{35}$$

The $m \times n$ matrix $\boldsymbol{F}$ consists of elements, F_{ij}, which are harmonic polynominals associated with the unknowns, X_i. It can be deduced that $F_{0j} = 1$ and $F_{ij} = [J^{\beta_i}(\theta_j) + R^{2\beta_i} J^{-\beta_i}(\theta_j)] \cos(\beta_i \theta)$ from Eq. (33). The boundary value problem, Eq. (34), can be solved using two methods: the point-match method and the least-squares-matching method (Shah, 1975). In the point-match method, the number of boundary points chosen for the solution equals the number of unknowns, X_i, i.e., $m = n$. On the other hand, in the least-squares-matching method, a larger number of boundary points are chosen for a better match of the curved or sharp-cornered boundaries. We use the point-match method to solve the present problem. Accordingly, the matrix $\boldsymbol{F}$ is changed to be a $n \times n$ matrix and the $\boldsymbol{X}$ in Eq. (34) has a set of exact solutions. The **LU**-decomposition (Bajpai et al., 1990) is employed to solve the linear equations subjected to Eq. (34) and the detailed steps are given as follows,

$$u_{1j} = F_{1j}, \quad j = 1, 2, \ldots, n; \tag{36}$$

$$l_{i1} = F_{i1}/u_{11}, \quad i = 2, 3, \ldots, n; \tag{37}$$

$$u_{kj} = F_{kj} - \sum_{m=1}^{k-1} l_{km} u_{mj}, \quad j = k, k+1, \cdots, n; \tag{38}$$

$$l_{ik} = \left(F_{ik} - \sum_{m=1}^{k-1} l_{im} u_{mk} \right) \Big/ u_{kk}, \quad i = k+1, k+2, \ldots, n; \tag{39}$$

$$z_1 = Y_1; \tag{40}$$

$$z_i = Y_i - \sum_{j=1}^{i-1} l_{ij} z_j, \quad i = 2, 3, \ldots, n; \tag{41}$$

$$X_n = z_n/u_{nn}; \tag{42}$$

$$\text{and} \quad X_i = \left(z_i - \sum_{j=i+1}^{n} u_{ij} X_j \right) \Big/ u_{ii}. \tag{43}$$

Finally, the unknown coefficients $\widetilde{A}$ and $\widetilde{C}_i$ are calculated from Eqs. (36)–(43). A closed-form solution for the velocity distribution is subsequently obtained by combining Eqs. (18) and (31) as

$$u(r,\theta) = G\left[\frac{R^2}{4} + \widetilde{A} - \frac{R^2}{2}\ln r + \sum_{i=1}^{N} \widetilde{C}_i (r^{\beta_i} + R^{2\beta_i} r^{-\beta_i}) \cos(\beta_i \theta)\right]. \tag{44}$$

As Laplace's equation is considered here, the maximum error will occur at the boundary points. Therefore, the deviation from the boundary values,

$$\Delta = \frac{1}{N}\sum_{j=1}^{N} G\left[\frac{R^2}{4} + \widetilde{A} - \frac{R^2}{2}\ln r_j + \sum_{i=1}^{N} \widetilde{C}_i (r_j^{\beta_i} + R^{2\beta_i} r_j^{-\beta_i}) \cos(\beta_i \theta_j)\right], \tag{45}$$

reflects the accuracy of the computed velocity profile.

Integrating Eq. (44) over the considered flow cross-sectional area, we obtain the flow rate of the liquid, $\overline{V}$, as

$$\overline{V} = \int_{A_l} u(r,\theta)\,\mathrm{d}A_l = G\eta, \tag{46}$$

where

$$\eta = \int_0^{(\pi-\alpha)/2} \int_R^{J(\theta)} \left[\frac{R^2}{4} + \widetilde{A} - \frac{R^2}{2}\ln r + \sum_{i=1}^{N} \widetilde{C}_i (r^{\beta_i} + R^{2\beta_i} r^{-\beta_i}) \cos(\beta_i \theta)\right] r\,\mathrm{d}r\,\mathrm{d}\theta. \tag{47}$$

It is clear from Eqs. (46) and (47) that the flow rate of the liquid, $\overline{V}$, can be obtained, provided that the meniscus radius, R, of the interfacial cross-section is known.

Since the liquid downflow results from the bubble upflow, the liquid flow rate, $\overline{V}$, depends on the bubble drift velocity, V_b. Based on the principle of mass conservation, the bubble drift velocity, V_b, is related to the liquid flow rate, $\overline{V}$, by

$$\overline{V} = -V_b(A_l - A_f) \tag{48}$$

where A_f is an unknown constant to be determined. Substituting Eq. (48) into Eq. (46) and then combining the result with Eq. (17) to eliminate G, we obtain

$$\frac{\mathrm{d}p_l}{\mathrm{d}z} = -\frac{\mu V_b}{\eta}(A_l - A_f) + (\rho_l - \rho_g)g. \tag{49}$$

Eq. (49) is also applicable in the uniform film zone, with $\mathrm{d}p_l/\mathrm{d}z = 0$, $A_l = A_{l,u}$, and $\eta = \eta_u$. Here $A_{l,u}$ is the cross-sectional area of the liquid phase in the uniform film zone, and can be determined from Eq. (6) or (7). As a result, in the uniform film zone, we have

$$A_f = A_{l,u} - \frac{\eta_u(\rho_l - \rho_g)g}{\mu V_b}. \tag{50}$$

Substituting Eq. (50) into Eq. (49) gives

$$\frac{\mathrm{d}p_l}{\mathrm{d}z} = -\frac{\mu V_b}{\eta}(A_l - A_{l,u}) + \left(1 - \frac{\eta_u}{\eta}\right)(\rho_l - \rho_g)g, \tag{51}$$

where the subscript "u" represents the parameters in the uniform film zone. Substituting Eq. (51) into Eq. (12), we obtain

$$\sigma\frac{\mathrm{d}}{\mathrm{d}z}\left\{\frac{\mathrm{d}^2\delta}{\mathrm{d}z^2}\Big/\left[1+\left(\frac{\mathrm{d}\delta}{\mathrm{d}z}\right)^2\right]^{3/2}+1\Big/R\left[1+\left(\frac{\mathrm{d}\delta}{\mathrm{d}z}\right)^2\right]^{1/2}\right\} = \frac{\mu V_\mathrm{b}}{\eta}(A_\mathrm{l}-A_\mathrm{l,u})-\left(1-\frac{\eta_\mathrm{u}}{\eta}\right)(\rho_\mathrm{l}-\rho_\mathrm{g})g, \tag{52}$$

where A_l, R, and η are related to δ and can be derived from Eqs. (4)–(7) and (47). Similarly, $A_\mathrm{l,u}$ and η_u are dependent on δ_u and can be derived from the same equations. It should be noted here that δ_u is the value of at δ at $z=0$. Thus, there are two unknowns, δ and V_b in Eq. (52), implying that an additional equation to reflect the relation between V_b and δ is needed to solve Eq. (52). In the present problem, there is a continuity requirement that all the fluid displaced by the front meniscus of the bubble should enter into the rear meniscus zone through the uniform film zone (Bretherton, 1961). Thus

$$-V_\mathrm{b}(A_\mathrm{c}-A_\mathrm{l,u})=\overline{V}_\mathrm{u}, \tag{53}$$

where A_c represents the one-sixth portion of the cross-sectional area of the triangular channel or the one-eighth portion of the cross-sectional area of the square channel and $\overline{V}_\mathrm{u}$ is the liquid flow rate in the uniform film zone. Noting that in the uniform film zone $\overline{V}=\overline{V}_\mathrm{u}$ and $A_\mathrm{l}=A_\mathrm{l,u}$, we combine Eqs. (48), (50) and (53) to obtain

$$V_\mathrm{b}(A_\mathrm{c}-A_\mathrm{l,u})=\frac{(\rho_\mathrm{l}-\rho_\mathrm{g})g\eta_\mathrm{u}}{\mu}. \tag{54}$$

Since both $A_\mathrm{l,u}$ and η_u are dependent on δ_u, Eq. (54) gives the relationship between V_b and δ_u.

By combining Eqs. (52) and (54) subject to the corresponding boundary conditions to the front meniscus zone and the rear meniscus zone, we can determine the respective interface profiles in the two zones. In the next section, we shall discuss how to obtain the interface profiles for the front meniscus and the rear meniscus zones.

Following Bretherton (1961), Martinez and Udell (1989), and Ratulowski and Chang (1989), the front meniscus is computed independently to determine the film thickness in the uniform film zone and the bubble drifty velocity before the rear meniscus zone can be determined. Subsequently, the analysis of the rear meniscus zone can be completed in an individual calculation using the previously determined film thickness left by the front meniscus zone for the same bubble drift velocity. Consequently, we first consider the front meniscus. Noting that Eq. (52) is a third-order differential equation, three boundary conditions are needed. The geometric continuity of the interface profile with respect to the end of the uniform film zone ($z=0$) gives

$$z=0: \quad \frac{\mathrm{d}\delta}{\mathrm{d}z}=0,\ \frac{\mathrm{d}^2\delta}{\mathrm{d}z^2}=0. \tag{55}$$

The third boundary condition can be obtained from the symmetry condition of the interface at the front tip of the bubble that coincides with the channel centerline, i.e.,

$$\delta = \frac{b}{2\cos(\alpha/2)} : \frac{\mathrm{d}\delta}{\mathrm{d}z} \to \infty. \tag{56}$$

The film thickness of the uniform film zone, the bubble drift velocity, and the interface profile in the front meniscus zone can be obtained by solving Eqs. (52) and (54) subject to the boundary conditions given by Eqs. (55) and (56). Subsequently, the boundary conditions of the rear meniscus zone can be given as

$$z = 0 : \delta = \delta_{\mathrm{u}} \tag{57}$$

$$\text{and} \quad \delta = \frac{b}{2\cos(\alpha/2)} : \frac{\mathrm{d}\delta}{\mathrm{d}z} = -\infty, \tag{58}$$

with a pressure continuity condition,

$$z = 0 : \frac{\mathrm{d}^2\delta}{\mathrm{d}z^2} \Bigg/ \left[1 + \left(\frac{\mathrm{d}\delta}{\mathrm{d}z}\right)^2\right]^{3/2} + 1 \Bigg/ R_{\mathrm{u}} \left[1 + \left(\frac{\mathrm{d}\delta}{\mathrm{d}z}\right)^2\right]^{1/2} = 1/R_{\mathrm{u}}. \tag{59}$$

It should be noted here that, in Eqs. (57) and (58), the location with respect to $z = 0$ is the start of the rear meniscus zone. The left-hand side of Eq. (59) represents the surface tension at the starting point, $z = 0$, of the rear meniscus zone and the right hand represents the surface tension in the uniform film zone where the surface tension remains constant. Then the interface profile in the rear meniscus zone can be solved from Eqs. (52) and (54) with the boundary conditions given by Eqs. (57)–(59).

3. Numerical treatment

Based on the equations presented in the preceding sections, we now outline the numerical calculation procedures. The calculation of the bubble drift velocity and the interface profile of bubble proceeds in a stepwise manner as follows:

(1) Assume a film thickness in the uniform film zone, δ_{u} and obtain the meniscus radius, R, from Eq. (4) or Eq. (5), solve Eq. (33) for the liquid velocity distribution around the bubble, then calculate the parameter, η_{u} from Eq. (47), and finally, obtain the bubble drift velocity, V_{b} from Eq. (54).
(2) Solve Eq. (52) subject to Eqs. (55) and (56) by the fourth-order Runge–Kutta method and simultaneously solve Eqs. (33) and (47) to obtain the interface profile in the leading meniscus zone.
(3) Repeat steps (1) and (2); the numerical process is terminated when the slope of the interface is larger than 10^4 at the channel centerline.
(4) Apply the previously predicted parameters, δ_{u}, η_{u}, and V_{b} to Eq. (52) to determine the interface profile in the rear meniscus zone.
(5) Assume a boundary value of $\mathrm{d}\delta/\mathrm{d}z$ at $z = 0$ and solve Eq. (52) subject to Eqs. (57)–(59) by the fourth-order Runge–Kutta method while simultaneously solving Eqs. (33) and (47) to obtain the interface profile in the rear meniscus zone.

(6) If the slope of the interface is smaller than 10^4 at the channel axis, repeat step (5); the numerical calculation procedure is halted when $d\delta/dz \geqslant 10^4$ at the channel axis.

4. Results and discussion

The mathematical model presented in the preceding section is now applied to predict the drift velocity of the Taylor bubble in vertical mini equilateral triangular and square channels. The hydraulic diameters of the channels range from 0.25 to 4.00 mm. Both water and methanol are considered to be the working fluids, and their essential thermophysical properties are listed in Table 1.

4.1. Bubble characteristics

Fig. 4 presents the front meniscus profile of the Taylor bubble in equilateral triangular channels with hydraulic diameters of 0.67 and 2.00 mm. Each front meniscus profile, plotted in dashed lines, is represented by the variation in the gas/liquid interface location, δ (the distance from the channel corner tip to the gas/liquid interface), with the bubble length. The solid lines in this figure represent the variation in the front meniscus radius, R with the bubble length. Starting from the uniform zone ($\delta = \delta_u$ at $z = 0$), δ is seen to increase gradually along the bubble length. Near the cap of the front meniscus, it exhibits a rapid increase toward the channel centerline at point B, where the gas phase disappears and the liquid phase occupies the whole cross-section of the channel. It should be recognized that point A in Fig. 4 represents the point at which $\delta = \Lambda$ (see Eq. (3)), i.e., the division between the circular gas flow and the deformed gas flow, as depicted by the cross-section B–B in Fig. 1. Before point A, the meniscus profile overlaps with the meniscus radius because $\delta = R$ for the equilateral triangular channel. The meniscus radius increases with the bubble length until point A. Afterwards, it decreases toward zero when the liquid phase occupies the whole cross-section of the channel. It is also clear from this figure that a reduction in the channel size from $D_h = 2.00$ to 0.67 mm results in a smaller δ and a shorter front meniscus. The behavior can be explained as follows. Previous investigations (Bretherton, 1961; Zukoski, 1966; Kolb and Cerro, 1993b) indicted that the behaviors of Taylor bubbles in vertical channels

Table 1
Physical properties of water and methanol

Water		
Interfacial tension, σ	0.0717	$N\,m^{-1}$
Density of liquid, ρ_L	1000	$kg\,m^{-3}$
Density of air, ρ_G	1.177	$kg\,m^{-3}$
Dynamics viscosity of liquid, μ	1.13×10^{-3}	$N\,s\,m^{-2}$
Methanol		
Interfacial tension, σ	0.0187	$N\,m^{-1}$
Density of liquid, ρ_L	751	$kg\,m^{-3}$
Density of air, ρ_G	1.177	$kg\,m^{-3}$
Dynamics viscosity of liquid, μ	3.26×10^{-4}	$N\,s\,m^{-2}$

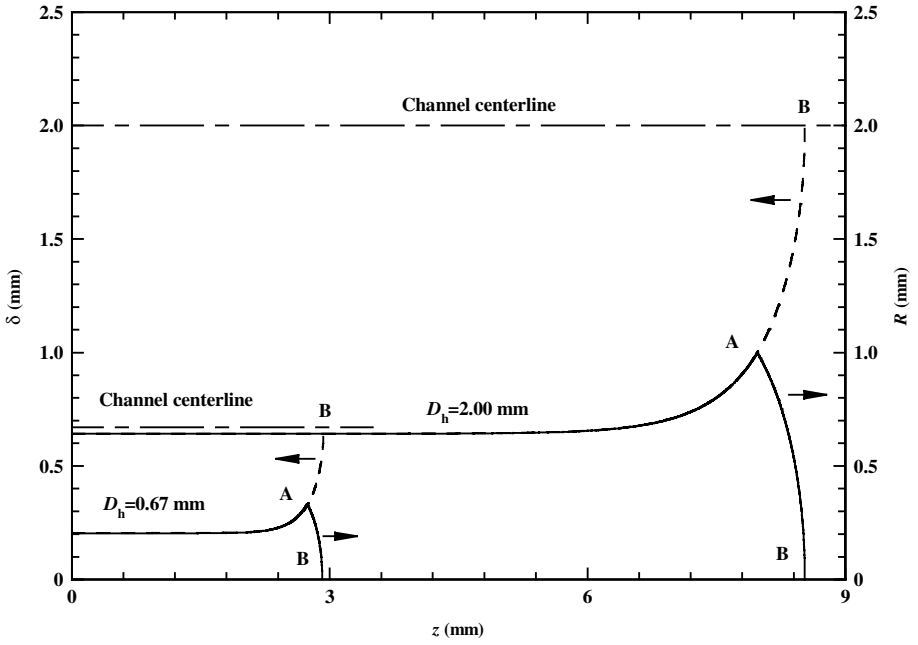

Fig. 4. Front meniscus profiles of the Taylor bubble in triangular channels.

depended on the capillary number, Ca, and the Eötvös number (or Bond number), $E\ddot{o} = \Delta\rho g d^2/\sigma$. The capillary number reflects the ratio of the viscous force to surface tension, while the Eötvös number represents the ratio of buoyancy force to the surface tension. As the channel size is reduced, the corresponding Eötvös number gets smaller, implying that the buoyancy force also becomes smaller. Thus, the velocity of the rising bubble decreases with a decrease in the channel size while the viscosity and the surface tension remain constant. A lower bubble drift velocity will result in a smaller flow rate of the downward liquid flow in the corner of the triangular channel. As a result, the area occupied by the liquid across the cross-section of the channel becomes smaller. Therefore, δ becomes smaller as channel size is reduced. A decrease of bubble drift velocity also induces a smaller Ca and thus, a smaller viscous force. The bubble interface profile will become flatter under the influence of a smaller viscous shear force. Consequently, the front meniscus becomes shorter with a decrease in the channel size.

The effects of the fluid properties on the front meniscus profiles in a triangular channel are presented in Fig. 5. As seen in this figure, in comparison with methanol, water as the liquid phase leads to a smaller δ and a longer front meniscus. This behavior is attributed to the fact that water has a larger surface tension than methanol has. A larger capillary force results in less liquid being retained in the corner of the channel.

Fig. 6 presents the rear meniscus profile in an equilateral triangular channel with a hydraulic diameter of 2.00 mm for both water and methanol. As compared with the front meniscus profiles shown in Fig. 4, the rear meniscus profile exhibits sharp variations at the gas/liquid interface with the bubble length and the rear meniscus zone is shorter than the front meniscus zone.

The bubble profiles in the uniform film zone are characterized by the cross-sectional area of the liquid-phase in the uniform film zone, $A_{l,u}$, or by the distance from the channel corner tip to the

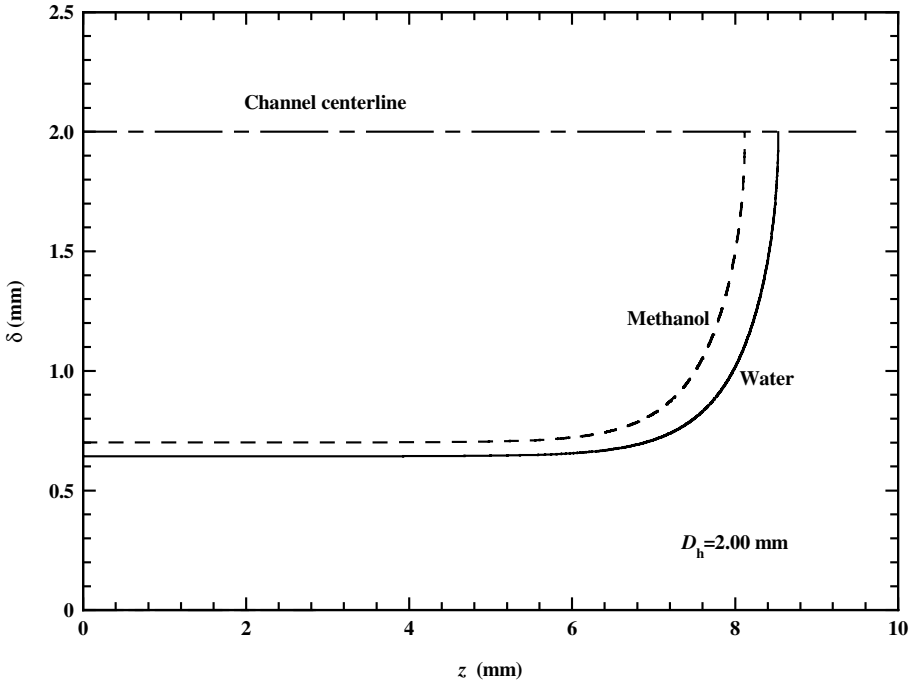

Fig. 5. Effects of the fluid physical properties on the front meniscus profile in triangular channels.

gas–liquid interface, δ_u. The variations in both $A_{l,u}$ and δ_u with the hydraulic diameter of the triangular channel are displayed in Fig. 7. As seen from this figure, both $A_{l,u}$ and δ_u increase with a increase in the channel size. Fig. 8 presents the variations in the cross-sectional area of the liquid phase in the uniform film zone, $A_{l,u}$, with the hydraulic diameter for water and methanol. As indicated in this figure, the liquid flow area of the uniform film zone for methanol is larger than that for water, because methanol has a smaller surface tension and a lower dynamic viscosity than water.

4.2. Bubble drift velocity

The bubble drift velocities, V_b predicted by the present model are compared with the experimental data presented by Bi and Zhao (2001) for water in equilateral triangular and square channels in Fig. 9. Eqs. (1) and (2), proposed, respectively, by White and Beardmore (1962) and by Tung and Parlange (1976) are also plotted in this figure for comparison. It can be seen from Fig. 9 that, compared with the previous models, the present model is more favorably in agreement with the experimental data, although there do exist some discrepancies between the theory and the experimental data for the triangular channel.

Fig. 9 also indicates that the bubble drift velocity increases with increasing channel size. As mentioned earlier, the larger Eötvös number corresponding to a larger channel results in a larger buoyancy force. Therefore, for a given pair of fluids, the bubble drift velocity increases with increasing channel size. Fig. 9 also shows that the drift velocity in the triangular channel is higher

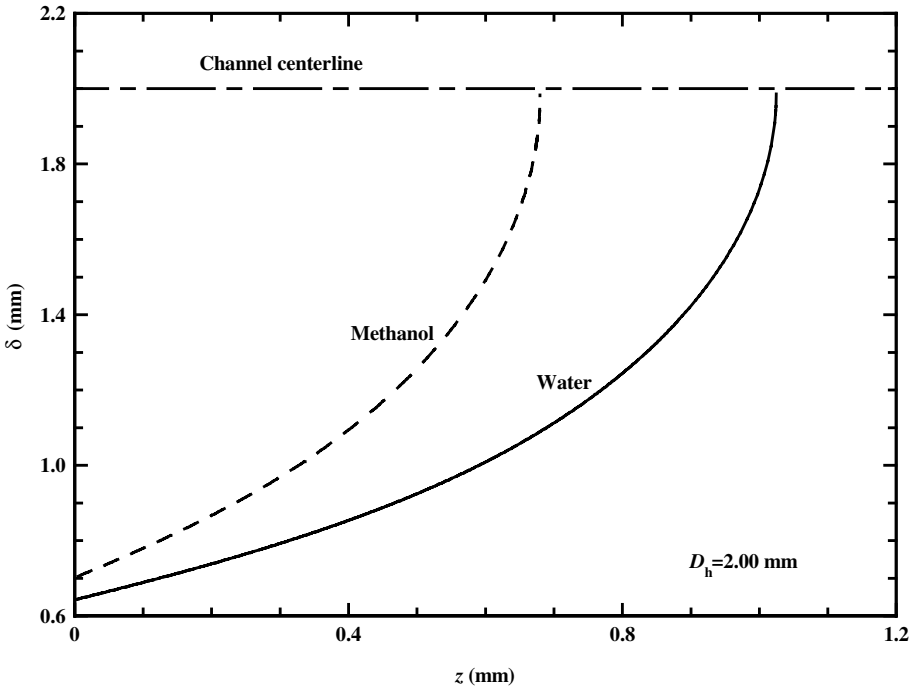

Fig. 6. Rear meniscus profiles of the Taylor bubble in triangular channels.

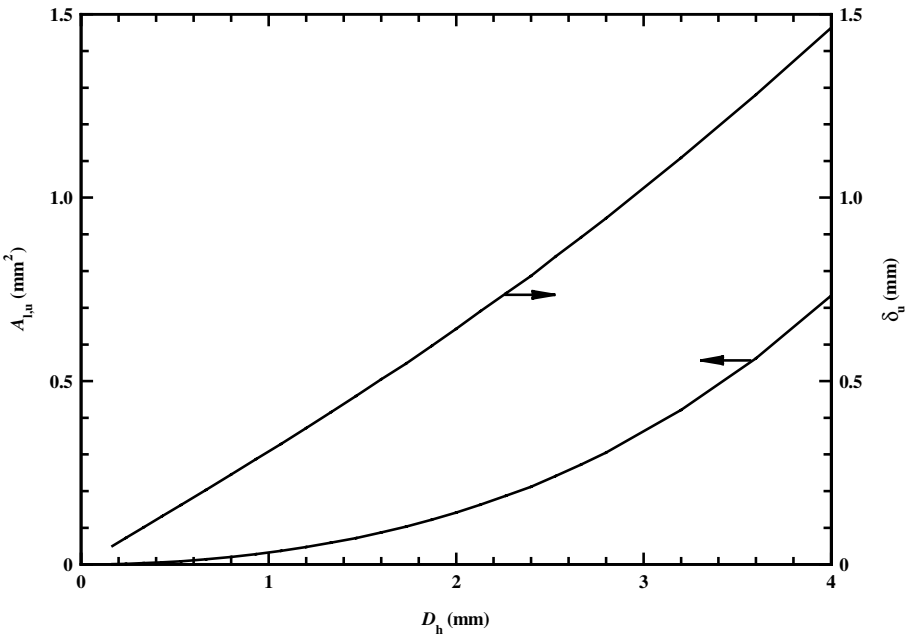

Fig. 7. Effects of the channel size on the gas/liquid location, δ_u, and the liquid flow area, $A_{l,u}$ in the uniform film zone in triangular channels.

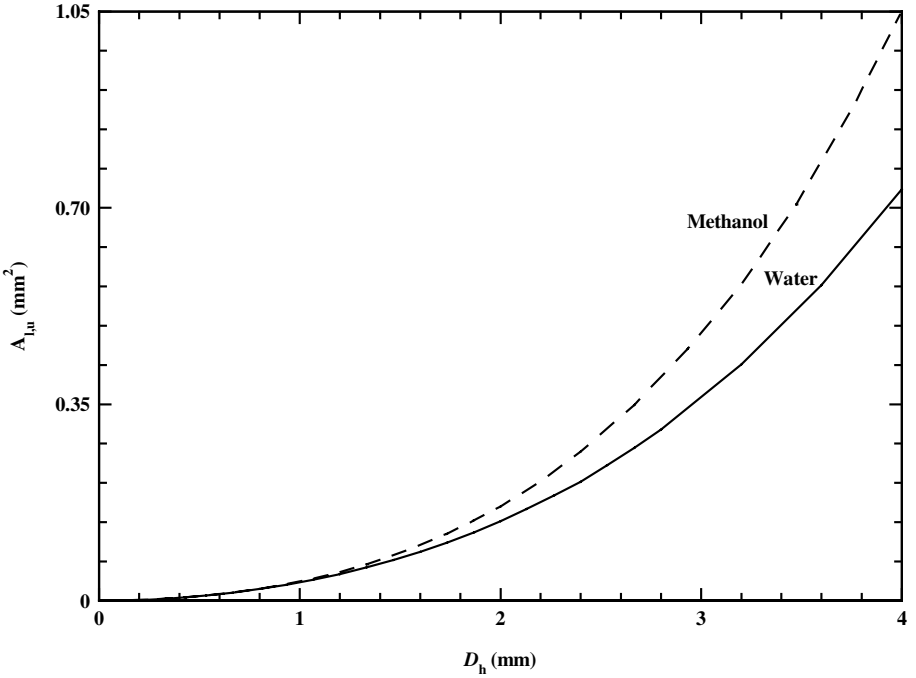

Fig. 8. Effects of the physical properties of liquids on the liquid flow area $A_{l,u}$ in the uniform film zone in triangular channels.

than in the square channel with the same hydraulic diameter, which is validated by the experimental data from Bi and Zhao (2001). The sharper corner of the triangular channel tends to retain more liquids in the corner as compared with the square channel, implying that the area occupied by the liquid in the triangular channel is larger than in the square channel. As a result, the flow rate of the downward liquid flow is higher for the triangular channel. The corresponding bubble drift velocity in the triangular channel is therefore higher than in the square channel having the same hydraulic diameter.

Fig. 10 presents the effects of the physical properties of liquids on the bubble drift velocity in both the triangular channel and the square channel. For the same channel shape and size, the bubble drift velocity in the liquid methanol is significantly larger than in the liquid water. This behavior is attributed to the fact that water has a larger surface tension than methanol. Thus, more water than methanol will be retained in the corner of the same channel. As a result, the flow rate of the downward water flow is higher than that of the methanol flow in the same channel. The corresponding bubble drift velocity for water is therefore higher than for methanol. In addition, the large dynamic viscosity of water may also lead to a lower drift velocity as compared with methanol.

Fig. 11 presents the effect of the physical properties of liquids on the liquid pressure differences between the bubble cap and the tail in the triangular channel. It can be seen that the pressure difference increases with an increase in the channel size for both water and methanol, which results from the fact that a larger channel results in a larger bubble drift velocity and thus a larger

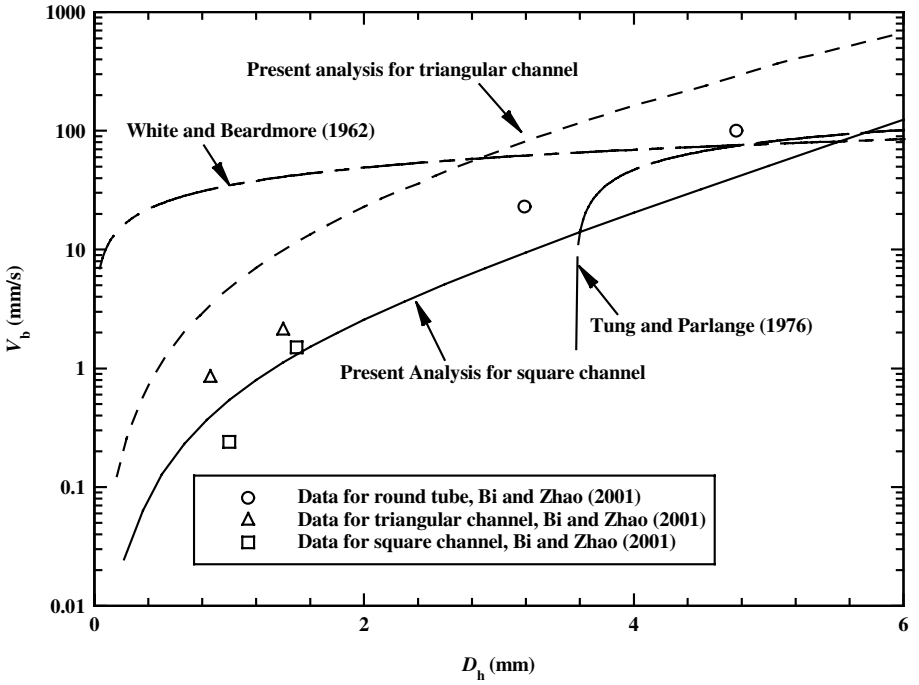

Fig. 9. Effects of the channel size on the bubble drift velocity.

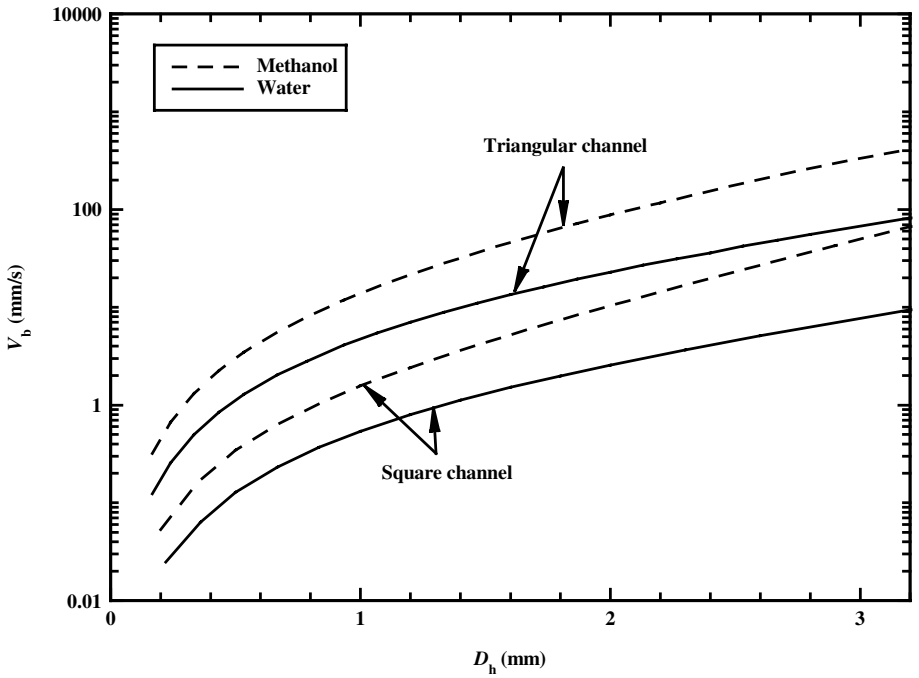

Fig. 10. Effects of the physical properties of liquids on the drift velocity of the bubble.

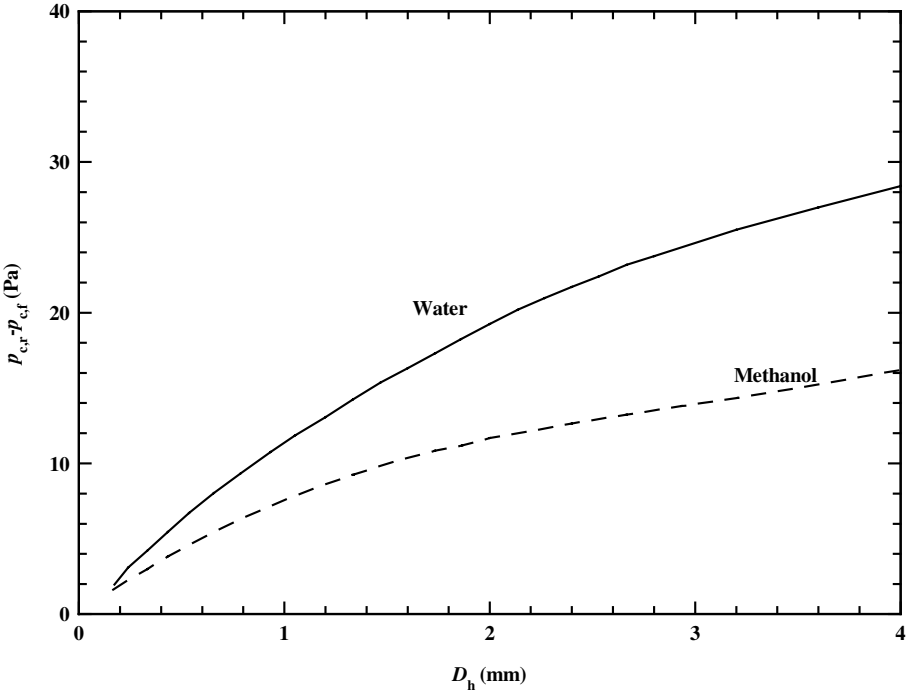

Fig. 11. Effects of the channel size and the physical properties of liquids on the liquid pressure difference between the cap and the tail of the bubble.

pressure loss. We can also see in this figure that the liquid pressure difference is larger for water than for methanol for the same channel size, which is mainly from the larger dynamic viscosity and surface tension of water. A larger surface tension leads to a smaller liquid flow area in the corner of the channel and thus, there is a larger viscous force. The liquid pressure difference increases with an increase in the dynamic viscosity.

4.3. Correlations of bubble drift velocity

In this section, we attempt to propose a simple correlation equation that predicts the drift velocity in both equilateral triangular and square channels. To this end, we rewrite Eq. (50) into a dimensionless form as

$$\frac{\mathrm{d}}{\mathrm{d}\bar{z}}\left\{\frac{\mathrm{d}^2\bar{\delta}}{\mathrm{d}\bar{z}^2}\Big/\left[1+\left(\frac{\mathrm{d}\bar{\delta}}{\mathrm{d}\bar{z}}\right)^2\right]^{3/2}+1\Big/\bar{R}\left[1+\left(\frac{\mathrm{d}\bar{\delta}}{\mathrm{d}\bar{z}}\right)^2\right]^{1/2}\right\}=-\frac{\bar{A}_\mathrm{l}-\bar{A}_\mathrm{l,u}}{\bar{\eta}}Ca+\left(1-\frac{\bar{\eta}_\mathrm{u}}{\bar{\eta}}\right)E\ddot{o}, \tag{60}$$

where D_h is the reference scale of the length for, δ, z, and R; D_h^2 the reference scale of the area for the cross-sectional area, A_l and $A_\mathrm{l,u}$; and D_h^4 is the reference scale for parameters η and η_u. Inspection of Eq. (60) indicates that the capillary number is dependent on the Eötvös number only

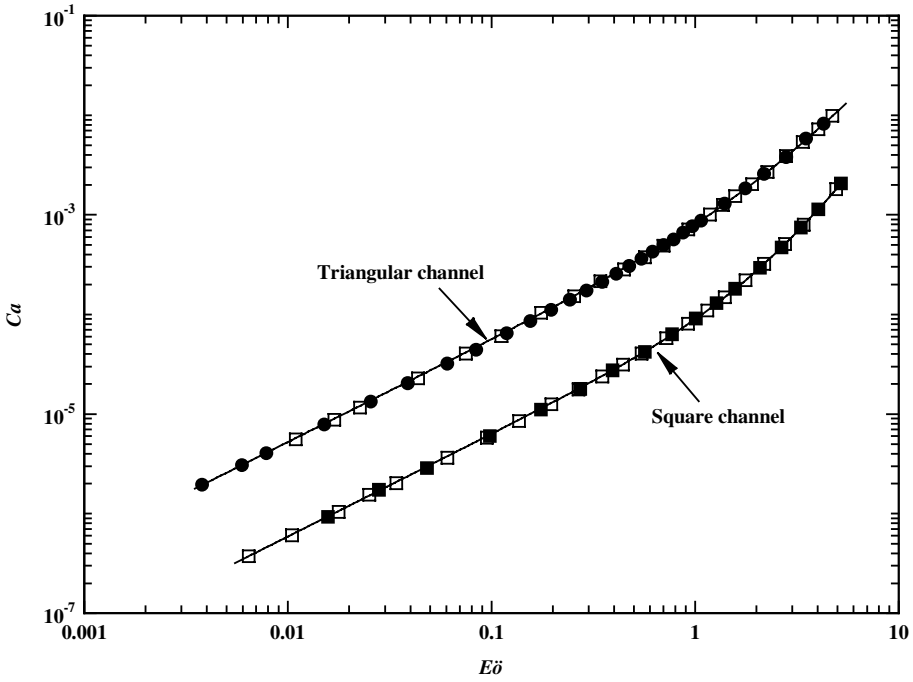

Fig. 12. Comparison of *Ca* predicted by the present analysis with the proposed correlations.

for a specific channel shape. Therefore, for a specific channel shape, the drift velocity can be predicted by correlating the capillary number, *Ca*, in terms of the Eötvös number *Eö*. The results of the computations for *Ca* vs. *Eö* for equilateral triangular channels are presented in Fig. 12, which can best be fitted by the following algebraic equation:

$$Ca = 0.0005800E\ddot{o}^{1.0226} + 0.0002223E\ddot{o}^{2.2203}. \tag{61}$$

The maximum relative deviation between Eq. (61) and the numerical results is about ±3.0% for the ranges of $1.95 \times 10^{-6} < Ca < 0.0099$, $0.0038 < E\ddot{o} < 4.73$, and $0.25 < D_h < 4.0$ mm. For square channels, the following equation:

$$Ca = 0.00006687E\ddot{o}^{1.0276} + 0.00002256E\ddot{o}^{2.6108}, \tag{62}$$

fits the numerical results well as shown in Fig. 12. The maximum relative deviation between Eq. (62) and the numerical results is about ±3.2% for the ranges of $3.67 \times 10^{-7} < Ca < 0.00207$, $0.0066 < E\ddot{o} < 5.21$, and $0.25 < D_h < 4.0$ mm.

5. Concluding remarks

An analytical model for predicting the drift velocity of a long inviscid bubble (a Taylor bubble) steadily creeping upwards in vertical mini triangular and square channels under the influence of buoyancy has been presented. The analysis is made by dividing the liquid flow field around the

bubble into the front meniscus zone near the leading edge of the bubble, the rear meniscus zone near the trailing edge of the bubble, and the uniform film zone in the middle. The effects of capillary force, gravity force, and viscous force have been incorporated in the model. It has been shown that the predicted bubble drift velocities are favorably in agreement with the experimental data reported in previous investigations of air bubbles in liquid water in both square and triangular mini channels. It has been revealed that the drift velocities in the triangular channel are substantially higher than that in the square channel having the same hydraulic diameter. The influences of channel size and the physical properties of liquids on the bubble drift velocities are also investigated. Finally, respective correlations for predicting the bubble drift velocities in both mini triangular and square channels have been developed in terms of appropriate dimensionless parameters.

Acknowledgements

This work was supported by Hong Kong RGC earmarked research grant no. HKUST 6178/00E and by the National Natural Science Foundation of China under grant no. 50006015.

References

Bajpai, A.C., Mustoe, L.R., Walker, D., 1990. Advanced Engineering Mathematics, second ed. John Wiley & Sons, New York.

Bendiksen, K.H., 1985. On the motion of long bubbles in vertical tubes. Int. J. Multiphase Flow 11, 791–812.

Bi, Q.C., Zhao, T.S., 2001. Taylor bubbles in miniaturized circular and noncircular channels. Int. J. Multiphase Flow 27, 561–570.

Bretherton, F.P., 1961. The motion of long bubbles in tubes. J. Fluid Mech. 10, 166–188.

Caetano, E.F., Shoham, O., Brill, J.P., 1992. Upward vertical two-phase flow through an annulus. Part I. Single-phase friction factor, Taylor bubble rise velocity, and flow pattern prediction. J. Energy Resour. Technol. 114, 1–13.

Collins, R., 1967. The effect of a containing cylindrical boundary on the velocity of a large gas bubble in a liquid. J. Fluid Mech. 28, 97–112.

Das, G., Das, P.K., Purohit, N.K., Mitra, A.K., 1998. Rise velocity of a Taylor bubble through concentric annulus. Chem. Eng. Sci. 53, 977–993.

Goldsmith, H.L., Mason, S.G., 1963. The flow of suspensions through tubes: II. Single large bubbles. J. Colloid Interf. Sci. 18, 237–261.

Kataoka, Y., Suzuki, H., Murase, M., 1987. Drift-flux parameters for upward gas flow in stagnant liquid. J. Nucl. Sci. Technol. 24, 580–586.

Kolb, W.B., Cerro, R.L., 1991. Coating the inside of a capillary of square cross section. Chem. Eng. Sci. 46, 2181–2195.

Kolb, W.B., Cerro, R.L., 1993a. Film flow in the space between a circular bubble and a square tube. J. Colloid Interf. Sci. 159, 302–311.

Kolb, W.B., Cerro, R.L., 1993b. The motion of long bubbles in tubes of square cross section. Phys. Fluids A 5, 1549–1557.

Legait, B., 1983. Laminar flow of two phases through a capillary tube with variable square cross-section. J. Colloid Interf. Sci. 96, 28–38.

Martinez, M.J., Udell, K.S., 1989. Boundary integral analysis of the creeping flow of longbubbles in capillaries. J. Appl. Mech. 56, 211–217.

Monde, M., 1990. Measurement of liquid film thickness during passage of bubbles in a vertical rectangular channel. ASME J. Heat Transfer 112, 225–258.

Nickens, H.V., Yannitell, D.W., 1987. Effects of surface tension and viscosity on the rise velocity of a larger gas bubble in a closed, vertical liquid-filled tube. Int. J. Multiphase Flow 13, 57–69.

Polonsky, S., Shemer, L., Barnea, D., 1999. Relation between the Taylor bubble motion and the velocity field ahead of it. Int. J. Multiphase Flow 25, 957–975.

Ransohoff, T.C., Radke, C.J., 1988. Laminar flow of a wetting liquid along the corners of a predominantly gas-occupied noncircular pore. J. Colloid Interf. Sci. 121, 392–401.

Ratulowski, J., Chang, H.C., 1989. Transport of gas bubbles in capillaries. Phys. Fluids A1 10, 1642–1655.

Reinelt, D.A., 1987. Rate at which a long bubble rises in a vertical tube. J. Fluid Mech. 175, 557–565.

Schwartz, L.W., Princen, H.M., Kiss, A.D., 1986. On the motion of bubbles in capillary tubes. J. Fluid Mech. 172, 259–275.

Shah, R.K., 1975. Laminar flow friction and forced convection heat transfer in ducts of arbitrary geometry. Int. J. Heat Mass Transfer 18, 849–862.

Stebe, K.J., Barthes-Biesel, D., 1995. Marangoni effects of adsorption–desorption controlled surfactants on the leading end of an infinitely long bubble in a capillary. J. Fluid Mech. 286, 25–48.

Thulasidas, T.C., Abraham, M.A., Cerro, R.L., 1995. Bubble-train flow in capillaries of circular and square cross section. Chem. Eng. Sci. 50, 183–199.

Tomiyama, A., Sou, A., Sakaguchi, T., 1996. Numerical simulation of a Taylor bubble in a stagnant liquid inside a vertical pipe. JSME Int. J. Ser. B—Fluids Thermal Eng. 39, 517–524.

Tudose, E.T., Kawaji, M., 1999. Experimental investigation of Taylor bubble acceleration mechanism in slug flow. Chem. Eng. Sci. 54, 5671–5775.

Tung, K.W., Parlange, J.Y., 1976. Note on the motion of long bubbles in closed tube influence of surface tension. Acta Mechanica 24, 313–317.

White, E.T., Beardmore, R.H., 1962. The velocity of rise of single cylindrical air bubbles through liquids contained in vertical tubes. Chem. Eng. Sci. 17, 351–361.

Wong, H., Radke, C.J., Morris, S., 1995a. The motion of long bubbles in polygonal capillaries. Part 1. Thin films. J. Fluid Mech. 292, 71–94.

Wong, H., Radke, C.J., Morris, S., 1995b. The motion of long bubbles in polygonal capillaries. Part 2. Drag, fluid pressure and fluid flow. J. Fluid Mech. 292, 95–110.

Yang, Z.L., Palm, B., Sehgal, B.R., 2001. Numerical simulation of bubbly two-phase flow in a narrow channel. Int. J. Heat Mass Transfer 45, 1579–1602.

Zukoski, E.E., 1966. Influence of viscosity, surface tension, and inclination angle on motion of long bubbles in closed tubes. J. Fluid Mech. 25, 821–837.